The Role of Cloud-Radiative Interaction in Tropical Circulation and the Madden-Julian Oscillation

Yuanyuan Huang[a] , Daehyun Kim[b,c] , Tian Zhou[d] , Xiaoming Shi[a,e]

[a] *Division of Environment and Sustainability, The Hong Kong University of Science and Technology, Hong Kong, China*

[b] *School of Earth and Environmental Sciences, Seoul National University, Seoul, South Korea*

[c] *Department of Atmospheric Sciences, University of Washington, Seattle, WA, USA*

[d] *College of Atmospheric Sciences, Lanzhou University, Lanzhou, Gansu, China*

[e] *Center for Ocean Research in Hong Kong and Macau, The Hong Kong University of Science and Technology, Hong Kong, China*

Corresponding author: Xiaoming Shi, shixm@ust.hk

ABSTRACT: Cloud-radiative interaction (CRI) is a fundamental process that modulates tropical circulation and intraseasonal variability, including the Madden-Julian Oscillation (MJO). In this study, we investigate how the mean state of the tropical atmosphere and MJO respond to CRI intensity changes and provide insights into the underlying mechanisms, using the aquaplanet configuration in the Community Earth System Model 2 (CESM2). By enhancing CRI through tuning the DCS parameter (an auto-conversion threshold size in Morrison and Gettelman (2008) cloud microphysics scheme), we demonstrate that CRI intensification is linked to a warmer troposphere, an augmented tropical moisture amount, strengthened Hadley Cell (HC), stronger trade winds, and a stronger equatorward intertropical convergence zone (ITCZ) with more clouds and precipitation, reflecting stronger cloud-radiation-circulation feedback. The intensified CRI also influences the signals within the MJO band, leading to the intensification and slower propagation of the simulated MJO-like mode. The MJO intensification is likely associated with the mean state changes that support the development of deep convection. Moreover, the CRI itself, especially the interaction with the longwave radiation, also directly influences the MJO's maintenance and propagation, more contributing to the maintenance and deceleration of column moist static energy (MSE) on intraseasonal timescales.

1. Introduction

Cloud-radiative interaction (CRI) is a broad definition of a dynamic and complex process in the Earth's atmosphere, involving intricate the entanglement of cloud properties and radiation budget. The level, thickness, distribution, and other internal properties of clouds interact with the shortwave (SW) radiation absorbed from the sun and the longwave (LW) radiation emitted by the Earth, producing distinct radiative feedback to the atmosphere. CRI is thereby recognized for its great importance in regulating diverse atmospheric processes and the weather or climate systems (e.g., Tao et al. 1996). The concept of CRI is sometimes similar to the cloud-radiative feedback.

CRI has been proposed as a nonnegligible factor that affects the global-scale atmospheric circulation through various physical processes, including dynamics and thermodynamics (e.g., Shaw 2019; Li et al. 2015; Ceppi and Hartmann 2015; Tian and Ramanathan 2003; Harrop and Hartmann 2016; Ceppi et al. 2014). Apart from the significant circulation variations in mid-latitude under the influence of CRI changes, such as subtropical jet (SJ) shift (e.g., Shaw 2019) and intensification (e.g., Li et al. 2015), the tropical atmospheric processes appear to be more susceptible to the CRI changes because net energy input to the global climate system and concentrated water vapor always colocate at the low latitudes, leading to frequent deep convection and extensive cloud coverage. Tian and Ramanathan (2003) suggest that CRI drives and maintains the Hadley and Walker circulations via a moist dynamic model. Harrop and Hartmann (2016) mainly focus on the tropical changes using the Clouds On-Off Klimate Intercomparison Experiment (COOKIE) and find that when CRI is turned on, the Hadley Cell (HC) strengthens, the intertropical convergence zone (ITCZ) contracts toward the equator (regarded as a reduction of the double ITCZ in numerical simulations) with higher values of precipitation, and the tropical atmosphere is moistened.

In addition to the tropical mean circulation, other smaller-scale atmospheric processes and systems are also controlled by CRI variation. These atmospheric processes and systems are often convectively coupled, in which the CRI plays its salient role through deep convective clusters and clouds. Many previous studies have highlighted the role of CRI in modulating the Madden-Julian Oscillation (MJO), a representative of convectively coupled tropical intraseasonal variability, first discovered by Madden and Julian (1971). Various in-depth studies of CRI effects on MJO provide theoretical and technical bases for a better understanding of MJO and better MJO simulations and predictions. For example, Kim et al. (2015) define a greenhouse enhancement factor (GEF) to measure CRI at different MJO stages and find a positive correlation between the GEF strength and climate models' fidelity in simulating the MJO. Crueger and Stevens (2015) make clouds transparent to radiation in four coupled climate models to eliminate the radiative effects on the clouds while retaining cloud microphysical processes. Their findings suggest that turning on the CRI leads to stronger MJO and slower propagation. Shi et al. (2018) control the LW CRI effects by prescribing zonally uniform LW heating rate. Their results show that enabling the CRI can influence the scale selection of MJO by strengthening low-wavenumber modes. Benedict et al. (2020) use the "cloud locking" method to isolate CRI impacts on MJO, showing that the disabled CRI suppresses the MJO and the larger-wavenumber features, consistent with the results of Crueger and Stevens (2015) and Shi et al. (2018) for MJO strength, while contrary to the significant growth of larger-than-wavenumber-1 signals when zonal asymmetry of LW radiative feedback is disabled in Shi et al. (2018). Some other opposite views, however, report that CRI has minor or negative impacts on the development and maintenance of MJO (e.g., Lee et al. 2001).

The differences observed in the impacts of CRI on MJO across various studies might be attributed to model- or method-dependency of the numerical experiments, but they could also arise from the climate system's complexity. Therefore, understanding how CRI affects MJO behavior and how it can be accurately represented in numerical models to improve the MJO simulation performance remains a pressing and popular topic, requiring further support from experiments and theoretical investigations.

In this study, we intend to investigate how CRI modulates tropical mean circulation and MJO using idealized aquaplanet simulations. The simpler aquaplanet model is often regarded as a useful idealization not only for studying global general circulation but also for studying tropical intraseasonal oscillations (Lee et al. 2001; Maloney et al. 2010; Leroux et al. 2016; Shi et al. 2018; Andersen and Kuang 2012). It provides an ocean-only lower boundary condition without land, vegetation, topography, or sea ice, and avoids the CRI effect on mean circulation and MJO being influenced by some complex processes, such as land-sea distribution and variable sea surface temperature (SST) patterns. Furthermore, we control the CRI intensity by tuning a sensitive cloud microphysical parameter, which sets our experiments apart from other approaches which may completely turn off the cloud-radiative effect, like COOKIE (Li et al. 2015; Harrop and Hartmann

2016), “cloud locking” (Benedict et al. 2020), or zonally uniform radiation prescribing (Lee et al. 2001; Shi et al. 2018).

In addition, according to the previous research, the changes in HC, equatorial wind, tropical moisture, and the moisture gradient are all regarded as crucial factors affecting MJO behaviors (e.g., Adames and Wallace 2015; Crueger and Stevens 2015; Kang et al. 2021; Rushley et al. 2023). For example, the mean state with stronger HC caused by the changes in Earth orbit parameters increases the MJO precipitation variance (Rushley et al. 2023), and the larger meridional moisture gradient may enhance the MJO propagation over the Maritime Continent in boreal winter (Kang et al. 2021). Nevertheless, given that the CRI changes can influence the mean circulation and MJO, it raises the question of whether alterations in mean circulation can serve as a linkage between CRI changes and MJO variability. We will further explore this question based on our simulations and attempt to explain the underlying physical mechanisms.

This manuscript is organized as follows. Section 2 describes the model and parameter details of our simulations as well as the MJO analysis method. Section 3 describes the climate mean state changes under the intensified CRI. Section 4 describes the MJO characteristic changes in our simulations and discusses the possible mechanisms of MJO changes. The summary of our results and further discussion follow in Section 5.

2. Model and Methods

a. Aquaplanet Model

In our study, we use the atmospheric component of Community Earth System Model version 2 (CESM2), Community Atmosphere Model version 6 (CAM6, Bogenschutz et al. 2018). The aquaplanet configuration is applied to make CAM6 run above the prescribed SST based on the Aqua-Planet Experiment (APE, Williamson et al. 2012). The SST pattern is the ”QOBS”, as defined in the APE. The maximum SST is 27 °C at the equator. The SST decreases gradually with latitude and is maintained at 0 °C between 60° and 90° in both hemispheres:

$$T(\phi) = \begin{cases} \frac{1}{2}\left(2 - \sin^4\varphi - \sin^2\varphi\right)\delta T + T_{\min}, & if|\phi| < \frac{\pi}{3} \\ 0, & otherwise \end{cases}, \tag{1}$$

where ϕ is latitude, $\varphi = \frac{\pi}{2}\frac{\phi}{\phi_{\max}}$, $\phi_{\max} = \frac{\pi}{3}$, $\delta T = T_{\max} - T_{\min}$, $T_{\max} = 27$, $T_{\min} = 0$. The SST distribution and meridional profile are shown in Figure 1.

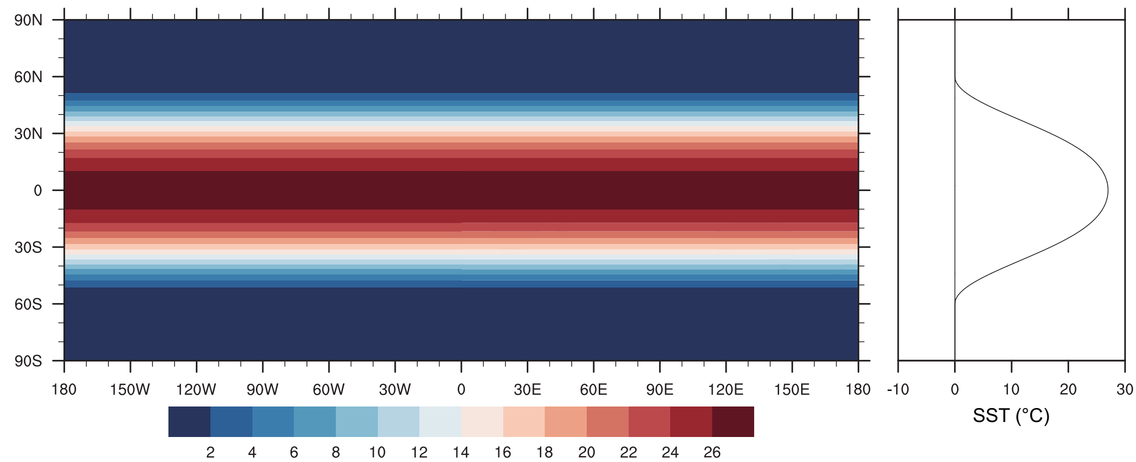

FIG. 1. SST global distribution and meridional profile (units: °C).

The default aquaplanet configuration in CAM6 adopts a finite volume (FV) dynamical core on a latitude-longitude grid with a horizontal resolution of 0.9° latitude × 1.25° longitude and 32 hybrid sigma-pressure levels. The model uses Cloud Layers Unified by Binormals (CLUBB, Golaz et al. 2002; Larson et al. 2002) scheme to parameterize the boundary layer, turbulence, shallow convection, and cloud macrophysics. The Zhang and McFarlane (1995) deep convection scheme and the Gettelman and Morrison (2015) cloud microphysics scheme are also adopted in the model. The radiative transfer is represented by the Rapid Radiative Transfer Model for General Circulation Models (RRTMG, Iacono et al. 2008). More aquaplanet-related details are documented in Medeiros et al. (2016).

b. DCS and Experiment Design

DCS refers to the auto-conversion threshold size defined in Equations (29) and (30) in Morrison and Gettelman (2008). In this cloud microphysics scheme, cloud ice and snow are separated into two categories. The DCS value determines when the auto-conversion from ice to snow takes place in numerical calculations. Smaller DCS values result in a more efficient conversion of cloud ice into snow, reducing the cloud ice. In contrast, larger DCS delays this conversion until the cloud ice particles grow to a larger size, causing more cloud ice to remain in the atmosphere. DCS is considered an effective turning parameter not only for tuning the model to reach its energy balance but also for investigating the specific scientific questions related to the cloud-radiative feedback (Zhao et al. 2013; Fan et al. 2021). The high sensitivity of cloud-radiative feedback to DCS has been demonstrated by Zhao et al. (2013), Eidhammer et al. (2014), and Pathak et al. (2020).

In this study, three main experiments are conducted by setting different DCS values in the CESM2 aquaplanet model. The default DCS value for CESM2 aquaplanet configuration is 500 µm, and the DCS values are set to 200 µm and 800 µm in two additional experiments. We name the three experiments DCS200, DCS500, and DCS800, respectively. All three experiments are integrated for ten years, with the first two-year simulation data discarded as spin-up, the last eight-year data considered as the stable state and used for analysis. The data are archived once a day.

c. CRI and Cloud Forcing

The concept of CRI in this manuscript is a broad definition, rather than a metric of a certain quantity. For example, some studies define a cloud-radiative feedback parameter to represent the role of CRI, which is often used in linear analytical models, such as Fuchs and Raymond (2002), Fuchs and Raymond (2005), Sobel and Maloney (2012), and Fuchs-Stone (2020).

In this study, we suggest that the smaller DCS causes the weaker CRI due to less cloud ice in the atmosphere, while stronger CRI is associated with larger DCS since more cloud ice has a stronger interaction with radiation.

We only care about the radiative effect on the atmosphere (not on the whole earth-atmosphere system or the surface) associated with clouds in this study. In some other studies, they also call it the atmospheric cloud-radiative effect (ACRE). When investigating the representation of CRI intensity, we calculate the cloud radiative forcing (hereafter called cloud forcing). The cloud forcing is calculated as the difference of column radiative convergence (the difference between net radiation flux at the top of the atmosphere and that at the surface) between the clearsky and cloudy conditions. The calculation of cloud forcing is considered the sum of the SW and LW components in order to present the total cloud-radiative effect, though the LW component is the main contributor to the total CRI (calculation not shown).

d. MJO-Associated Regression

The linear regression method (Adames and Wallace 2014, 2015) is applied to analyse the spatial structure of MJO-like disturbances, and the equation is as follows:

$$\mathbf{D} = \mathbf{S}\widehat{\mathbf{P}}^{\mathrm{T}}/N \tag{2}$$

where $\mathbf{D}$ is the regression results with the dimensional units, $\mathbf{S}$ is a two-dimensional matrix of the variable S, $\widehat{\mathbf{P}}$ is the time series of the MJO index, N is the sample size of the daily archived variable S, and the superscript T represents the transposition of a matrix.

The MJO index is calculated as follows: we select an approximate $5^\circ \times 5^\circ$ square box of precipitation rate centered at 180° on the equator. Then, we spatially average the precipitation rate in this region and standardize the resulting time series. A 20 to 100-day bandpass filter is also applied.

3. CRI-Induced Mean State Changes

a. Climate Mean State

Through tuning DCS in the CESM2 aquaplanet model, the climate mean state, including the thermodynamic conditions and large-scale circulations, presents discernible changes in the time-and-zonal-averaged plots. In this study, we mainly discuss those changes in the tropical atmosphere.

The air temperature changes with DCS are shown in the upper row of Figure 2. When DCS is tuned larger, the tropical tropospheric temperature significantly increases, particularly in the upper troposphere (around 300-hPa) and the height of tropical tropopause becomes higher. Such tropospheric warming may be attributed to the enhanced condensational heating and radiative heating and we will further discuss it in the following text. The tropical warming also leads to a larger temperature meridional gradient, driving a stronger poleward meridional heat transport. This warming pattern shares some similarities with greenhouse gas-caused warming in that the upper troposphere warms faster than the lower troposphere.

Figure 2d-f show the fractional changes of moisture with DCS. The moisture amount generally expands with increasing DCS in the deep tropics, especially having larger fractional changes in the middle and higher troposphere. It means that more moisture transports upward from the boundary

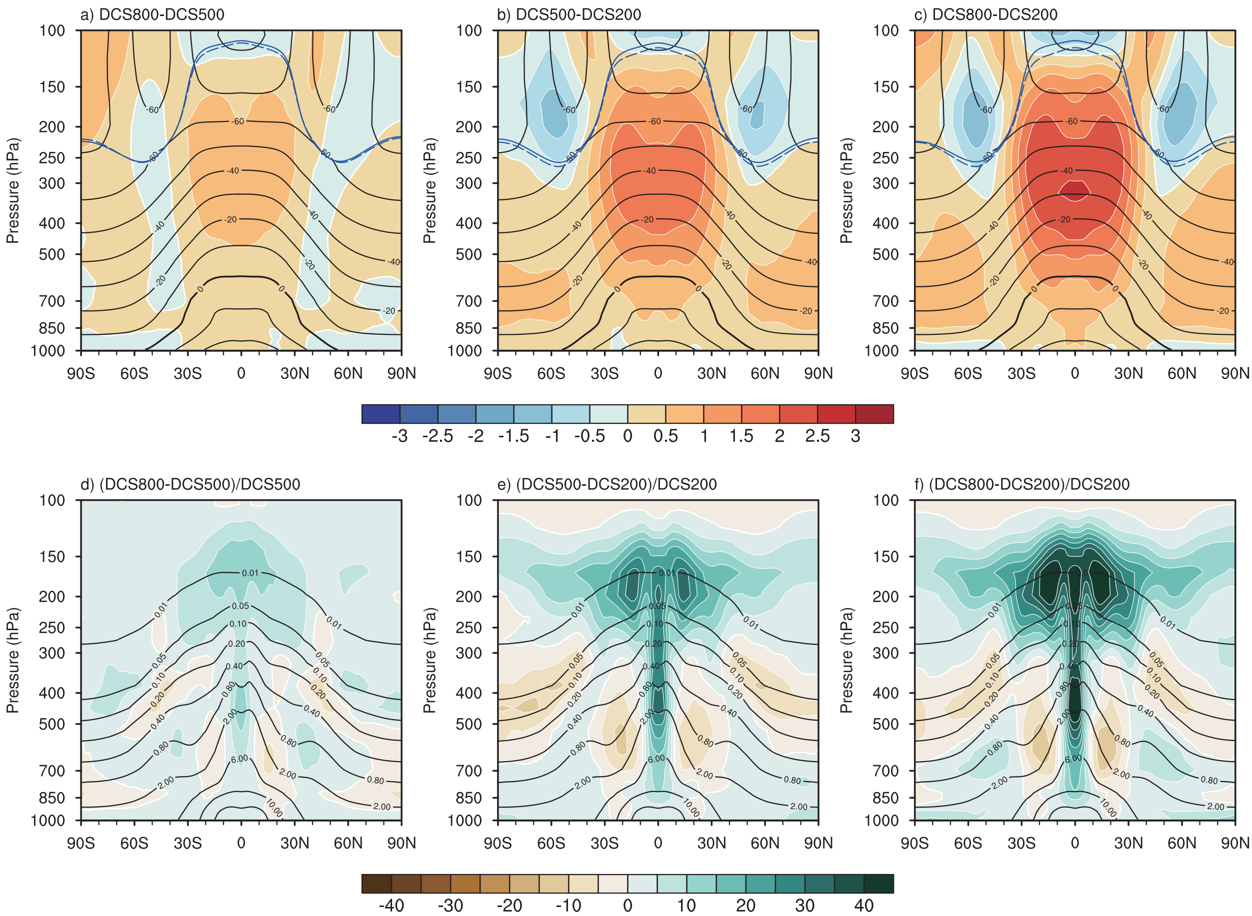

FIG. 2. (a, b, c) The changes of climatological zonal-averaged air temperature (color, units: °C) and (d, e, f) the fractional changes of climatological zonal-averaged specific humidity (color, units: %) between different cases. The climatological zonal-averaged air temperature and specific humidity of the DCS500 case are plotted as a reference (contour, units: °C for air temperature and g/kg for specific humidity). The interval of temperature contour is 10 °C and the interval of specific humidity contour is not evenly spaced (0.01, 0.05, 0.1, 0.2, 0.4, 0.8, 2, 6, 10, 14). The overlaid blue curves in the upper row represent the height of the tropopause. The blue solid curves are calculated in the larger-DCS case, and the blue dashed curves are calculated in the smaller-DCS case.

layer to the higher altitudes and converges therein. We also notice that there is a moisture decrease between 10°S/N-30°S/N outside the deep tropics, enhancing the meridional moisture gradient between deep tropics and subtropics.

Figure 3 depicts the time-mean, zonal-mean meridional mass stream function (MMSF), cloud fraction, and zonal wind with varying DCS values. As DCS increases, more cloud ice in the tropical atmosphere leads to a larger cloud fraction (the left column of Figure 3), particularly in the

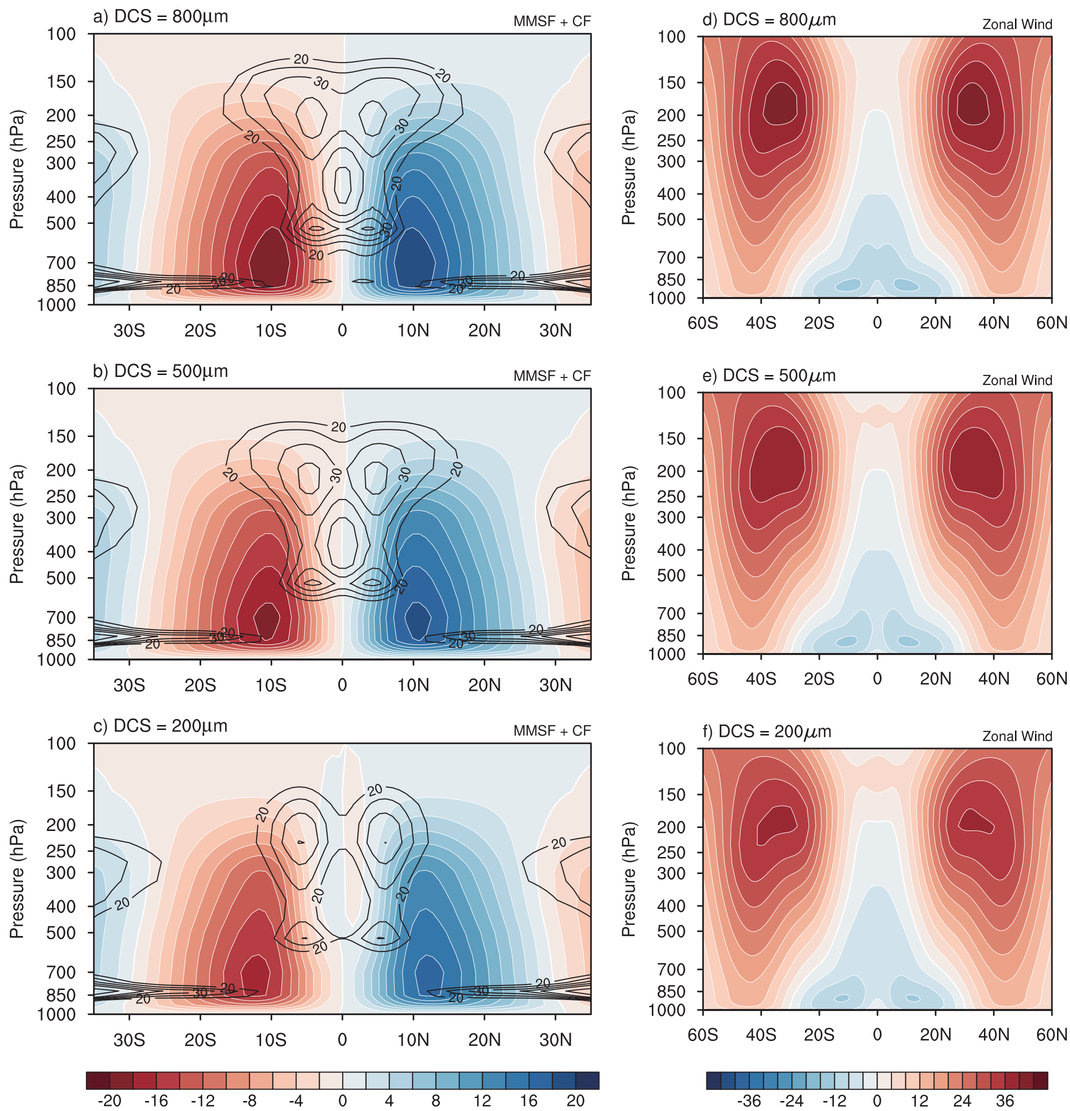

FIG. 3. The climatological zonal-averaged (a, b, c) meridional mass stream function (MMSF, color, units: 10^{10} kg/s) and cloud fraction (contour, units: %), and (d, e, f) zonal wind (units: m/s). The positive MMSF represents the clockwise circulation, while the negative MMSF represents the counter-clockwise circulation. The interval of the cloud fraction contour is not evenly spaced (20, 25, 30, 35, 40, 50, 60).

middle and upper troposphere. Concurrently, the positive/negative MMSF in the lower latitudes of the Northern/Southern Hemisphere (NH/SH) intensifies with increasing DCS, reflecting the strengthening of the HC. The change in HC also explains the moisture distribution change in Figure 2. The deep tropics moistening is due to the strengthening of the ascending branch of the

HC, and drying in the subtropical mid-troposphere is due to the strengthening of the descending branch.

The right column of Figure 3 shows the zonal wind changes in different experiments. When DCS increases, the SJ, the trade winds, and the equatorial low-level easterly strengthening are likely a result of the enhanced baroclinicity (equator-to-pole temperature gradient) and HC intensification, which enhances poleward transport of momentum. The averaged easterlies below 700-hPa within 5°S-5°N are 7.76 m/s, 6.90 m/s, and 5.18 m/s for the simulations of DCS800, DCS500, and DCS200, respectively.

b. Forcings Causing the Changes

In the tropical atmosphere, diabatic heating primarily arises from two major sources: atmospheric radiative heating and condensational heating. Tuning the DCS parameter directly alters the cloud-radiative effect, which can be represented by the changes in cloud forcing in Figure 4a. The cloud forcing significantly increases in the tropics with DCS, leading to stronger cloud radiative heating. To be specific, the deep-tropical (5°S-5°N) averaged cloud forcing is 16.94 W/m^2, 29.41 W/m^2, and 34.16 W/m^2 for DCS200, DCS500, and DCS800, respectively. It increases by 101.7 % from DCS200 to DCS800. The tropical atmosphere is heated by CRI intensification, which may contribute to the changes in tropical temperature and its meridional gradient in Figure 2. Meanwhile, the strengthened HC (Figure 3) is associated with the enhanced meridional temperature gradient and stronger meridional heat transport since HC is a thermal-driven overturning circulation. The study of Bischoff and Schneider (2016) and that of Harrop and Hartmann (2016) suggest that the stronger HC occurs when the equatorial energy input is larger, consistent with our results. It is worth noting that the atmospheric mean state, diabatic forcings, and other climate systems are all coupled, and the changes in HC can also feedback to the cloud forcing and temperature changes.

However, cloud forcing cannot be zonally symmetric. Thus, it should be made clear that the changes in Figure 4a are introduced by changing the clouds of individual convection systems, which collectively change the mean state of the atmosphere.

Figure 4b shows the climatological latitudinal precipitation distribution. By tuning DCS larger, the precipitation increases in the deep tropics with two peaks on both sides of the equator, exhibiting a stronger and narrower ITCZ. Further calculation shows that the averaged precipitation rate

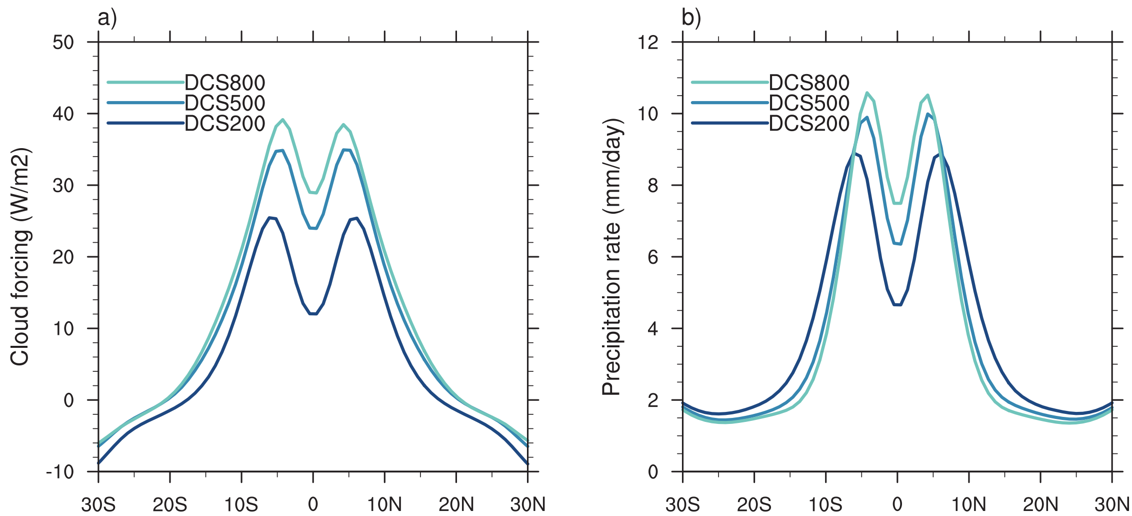

FIG. 4. The climatological zonal-averaged (a) total cloud radiative forcing (units: W/m^2), and (b) precipitation rate (units: mm/day). Positive cloud forcing values indicate radiative heating.

within 5°S-5°N is 6.17 mm/day, 8.18 mm/day, 9.19 mm/day for DCS200, DCS500, and DCS800, respectively, increasing by 48.9 % from DCS200 to DCS800. The location and the strength of ITCZ are closely related to the HC changes (Ceppi et al. 2013; Bischoff and Schneider 2016). In our simulations, the stronger and equatorward HC shift corresponds well to the ITCZ changes. The changes in HC enhance dynamical conditions for ITCZ and the increased radiative heating as well as moisture amount also directly provide the thermodynamic conditions. Similar results have been demonstrated by Harrop and Hartmann (2016), who suggest that ITCZ contracts toward the equator when turning on the CRI.

To show more details of the changes in the distributions of cloud forcing and precipitation within the tropics, and to better understand the role of DCS, Figure 5a presents the probability density function (PDF) of tropical cloud forcing. We can see that the changes in tropical cloud forcing with DCS mainly show a higher frequency of large cloud forcing events, especially the part larger than 100 W/m^2. It seems that the increased probability of large cloud forcing dominantly accounts for the mean cloud forcing changes while the weak cloud forcing has less contribution. As to the changes in tropical precipitation PDF distribution, Figure 5b shows that the median of probability shifts to the heavier precipitation in the tropics with the increasing DCS. The enhanced CRI leads to the increased probability of heavy precipitation and decreased probability of weak precipitation.

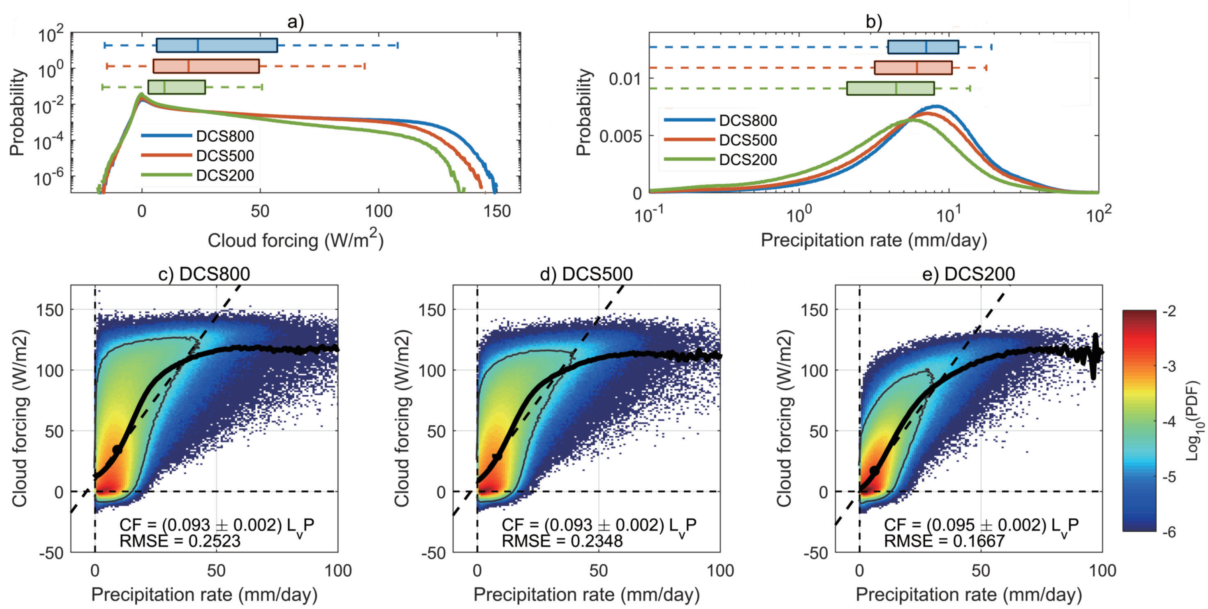

FIG. 5. The comparison of probability density function (PDF) of (a) tropical (5°S-5°N) total cloud radiative forcing (units: W/m^2) and tropical precipitation rate (units: mm/day) for different DCS cases. The y-axis in (a) and the x-axis in (b) are on a log scale. Boxplots of different DCS cases are shown over the PDF curves. The left and right edges of the box indicate the 25th and 75th percentiles. The vertical lines in the boxes are the median. The whiskers extend to a maximum of $1.0 \times$ interquartile range beyond the boxes. (c, d, e) The joint PDF of tropical precipitation rate (units: mm/day) and tropical cloud forcing (units: W/m^2) with varying DCS. The probability density is scaled by $\log_{10}$. The black dots correspond to the mean precipitation rate and mean cloud forcing. The black dashed lines indicate the linear regression of all colored bins. The thick black solid lines indicate the averaged cloud forcing binned by precipitation rate. The value of gray contours is -4.5, representing the region of relatively high probability density.

The extremely large values do not dominate the mean precipitation changes due to the probability being more concentrated in its median, following a log-normal distribution-like pattern.

The joint PDF in Figure 5c-e illustrates the changes in the radiation-precipitation (R-P) relation. This cloud forcing and precipitation do not follow a linear relationship, exhibiting an “S” shape (refer to the black solid curves in joint PDF plots). Near the median (black dots), the cloud forcing increases very fast with the precipitation increase. If we perform a linear regression between cloud forcing and precipitation rate within the gray contour of $\log_{10}$(PDF) = -4.5, the slopes are 0.106, 0.113, and 0.116 for DCS200, DCS500, and DCS800 respectively. The slopes are unitless since the units of precipitation are set to watts per square meter by multiplying the latent heat of vaporization L_v. Obviously, the slope increases from DCS200 to DCS800, which means the cloud forcing grows faster with increasing precipitation, leading to a stronger cloud-radiative effect per unit precipitation.

However, if the linear regression is performed among all colored bins, the slope from DCS200 to DCS800 does not change much (decreases from 0.095 to 0.093), which is contributed by the fact that the cloud forcing saturates when precipitation becomes very strong. The cloud forcing distribution can not further grow when precipitation increases with the strongest cloud forcing being limited below 150 W/m^2.

We still notice that the highest probability density regions with dark red are located at the lower left of black dots, away from the mean values. In spite of the lighter red color with the increasing DCS, the highest probability density regions do not have significant shifts following the shift of mean values. Accordingly, the black dot becomes farther away from the red region, and the probability density distribution becomes more dispersed, leading to larger variability.

Based on the analyses of Figure 5 above, the changes in cloud forcing can be partially reflected in the non-linear R-P relation changes. Although the R-P relation does not change substantially, the probability density of cloud forcing distributes more towards the regions with extremely large values in all rainfall range, making the “S” shape has a larger curvature with increasing DCS. Nonetheless, the cloud forcing can not grow infinitely with the precipitation increase. It also reflects that increasing CRI intensity by tuning DCS has limits, especially when DCS is extremely large.

The large cloud forcing is likely associated with deep convection or the stratiform region of the convective systems, which can be inferred from the statistical relationship between cloud forcing and precipitation (black solid lines in Figure 5c-e). If we separate the LW and SW components of cloud forcing (figure not shown), it is obvious that the large cloud forcing mainly comes from the LW component which is often associated with high clouds. It is understandable because we adjust the only process related to cloud ice. Cloud ice changes mainly occur in the cold upper troposphere where the deep convection can reach.

In our simulations, the changes in cloud forcing are firstly caused by the varying cloud microphysical processes through the DCS tuning. Larger DCS delays snow generation until ice particles grow to a larger size and thereby keeps more cloud ice in the atmosphere. The increased cloud ice induces stronger CRI, strengthening the cloud forcing but with an upper limit. Consequently, mean cloud forcing changes.

On the other hand, the changes in cloud forcing could be partially attributed to the mean state changes: warming and moistening of the tropical atmosphere strengthen HC, favorable for the development of deep convection in the tropical atmosphere and the generation of convective clouds. The increased cloud cover results in stronger cloud forcing, which, in turn, provides feedback to the mean state. This establishes a cloud-radiative-circulation feedback mechanism.

4. MJO Responses to CRI Changes

a. MJO Characteristics Changes

The Wheeler-Kiladis wavenumber-frequency spectra (Wheeler and Kiladis 1999, hereafter WK99) of tropical precipitation are shown in Figure 6 to qualitatively measure the characteristics of the MJO-like signal in the CESM2 aquaplanet simulations. Significant power exists within the "MJO band" (eastward propagation; wavenumber one to three; period of 20 to 100 days) in the WK99 spectra, peaking at wavenumber one. In both the symmetric and normalized (symmetric/background) spectra, MJO-like signal power extends to higher wavenumbers and shifts to lower frequencies with increasing DCS. The growth of higher-wavenumber signals may imply a smaller horizontal scale.

To see the frequency changes more clearly, we averaged the power of wavenumber one to three and fit the resulting power-frequency relation to a third-order polynomial around the intraseasonal frequency (Figure 7). On the symmetric spectra, the peak periods are 45, 41, and 34 days for the simulations of DCS800, DCS500, and DCS200, respectively. Therefore, the stronger CRI associated with larger DCS indeed leads to slower propagation of MJO-like mode.

However, it should be noted that the power at wavenumber one in the symmetric and normalized spectra is represented differently with the changes in CRI intensity. The power within the MJO band in the normalized spectra becomes weaker when DCS is higher, but the opposite trend exists in symmetric spectra. The reason is that the high DCS experiment exhibits stronger eastward background power in a wide eastward-wavenumber range, thereby making the normalized power weaker than the experiments with lower DCS values (figure not shown). The weaker wavenumber-1

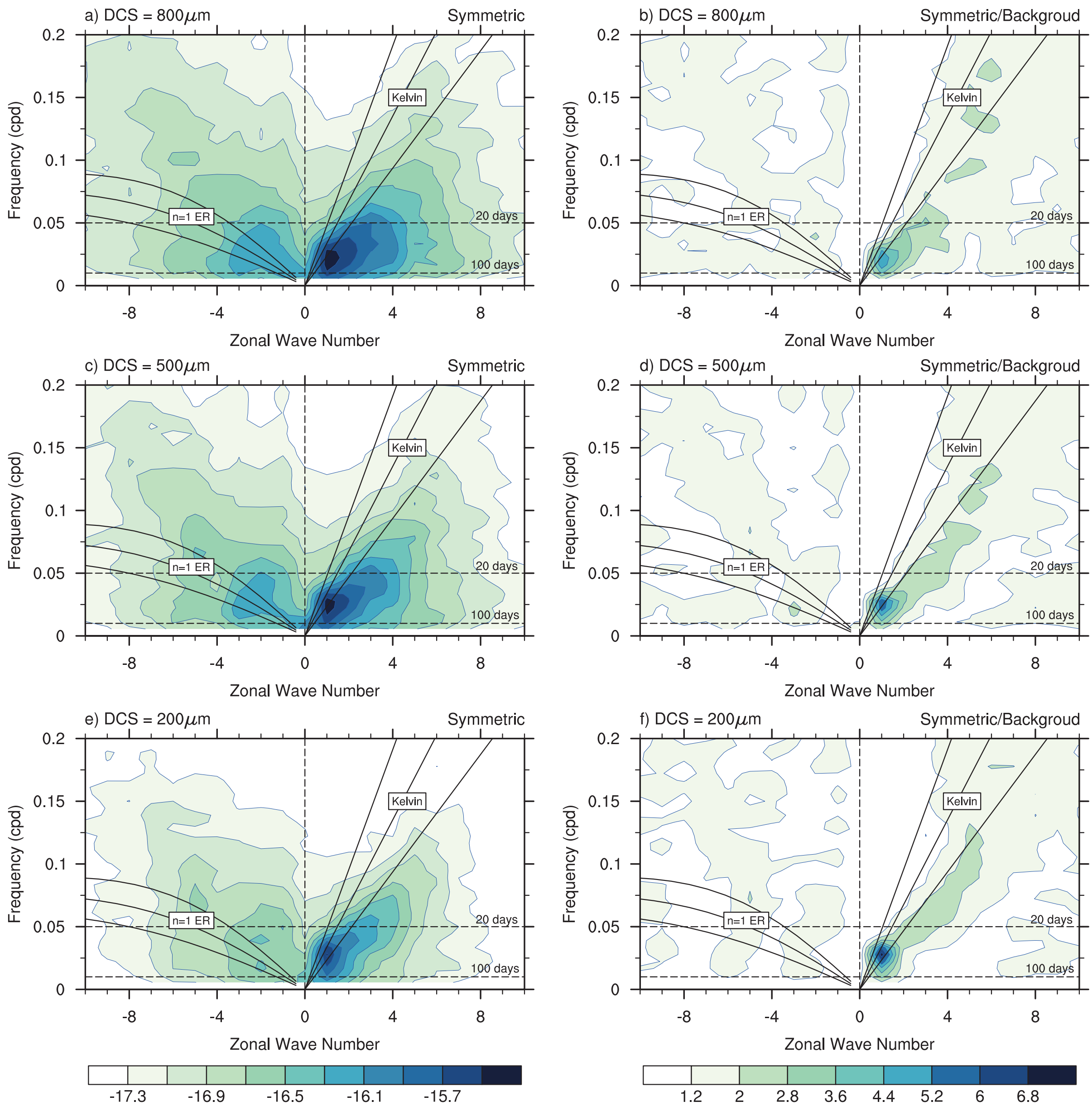

FIG. 6. The wavenumber-frequency spectra of precipitation rate within 5°S-5°N: (a, c, e) the symmetric spectra scaled by $\log_{10}$ and (b, d, f) the normalized spectra (symmetric power divided by background power). The superimposed black solid lines are the dispersion curves. The temporal window length is 200 days, and the overlapping temporal segments are 90 days.

signals and stronger higher-wavenumber signals in a relative sense reflect the scale selection issue. Nevertheless, the wavenumber one signal generally grows under the stronger CRI, intensifying MJO-like mode in our simulations.

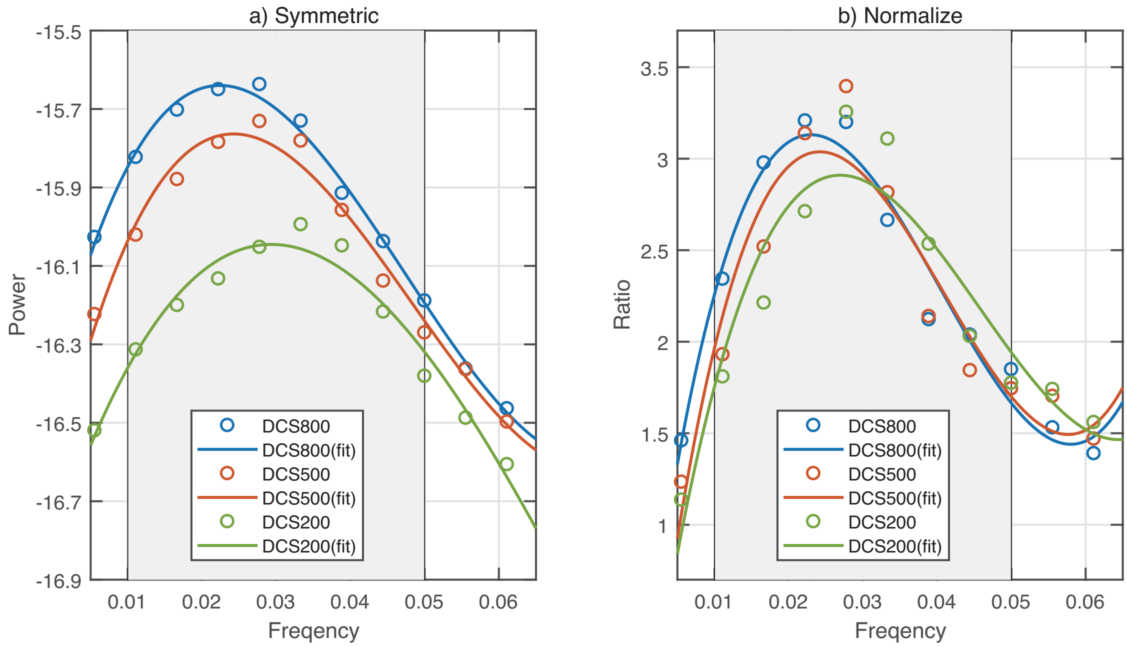

FIG. 7. (a) The power changes with frequency and their polynomial fitting curves in symmetric spectra. The frequency at the maximum power is 0.022 cpd (44.64 days), 0.024 cpd (41.15 days), and 0.029 cpd (34.13 days), corresponding to DCS800, DCS500, and DCS200, respectively. (b) The ratio changes with frequency and their polynomial fitting curves in normalized spectra. The frequency at the maximum ratio is 0.023 cpd (43.48 days), 0.024 cpd (41.32 days), and 0.027 cpd (37.04 days), corresponding to DCS800, DCS500, and DCS200 respectively.

In the regression maps (Figure 8), all fields represent approximate wavenumber one spatial structure centering at (0°, 180°) where the positive precipitation anomalies (left column) and the negative OLR (right column) anomalies are at maximum values. The regressed precipitation fields exhibit weak "swallowtail" shapes to the west of heavy precipitation centers, consistent with the observational MJO (Zhang and Ling 2012; Adames and Wallace 2015). From the low-level wind fields and stream function fields (left column), it is apparent that the CESM2 aquaplanet model can well produce the poleward anomalous flows to the east of convective centers and the wind-convection coupling in 850-hPa without phase differences, superior to some simulations (Zhang 2005; Shi et al. 2018) that simulate the unrealistic poleward flows or unrealistic convergence to the west of convective centers. The high-level wind and stream function in the right column of Figure 8 also shows relatively reasonable wind-convection coupling compared to the observational MJO.

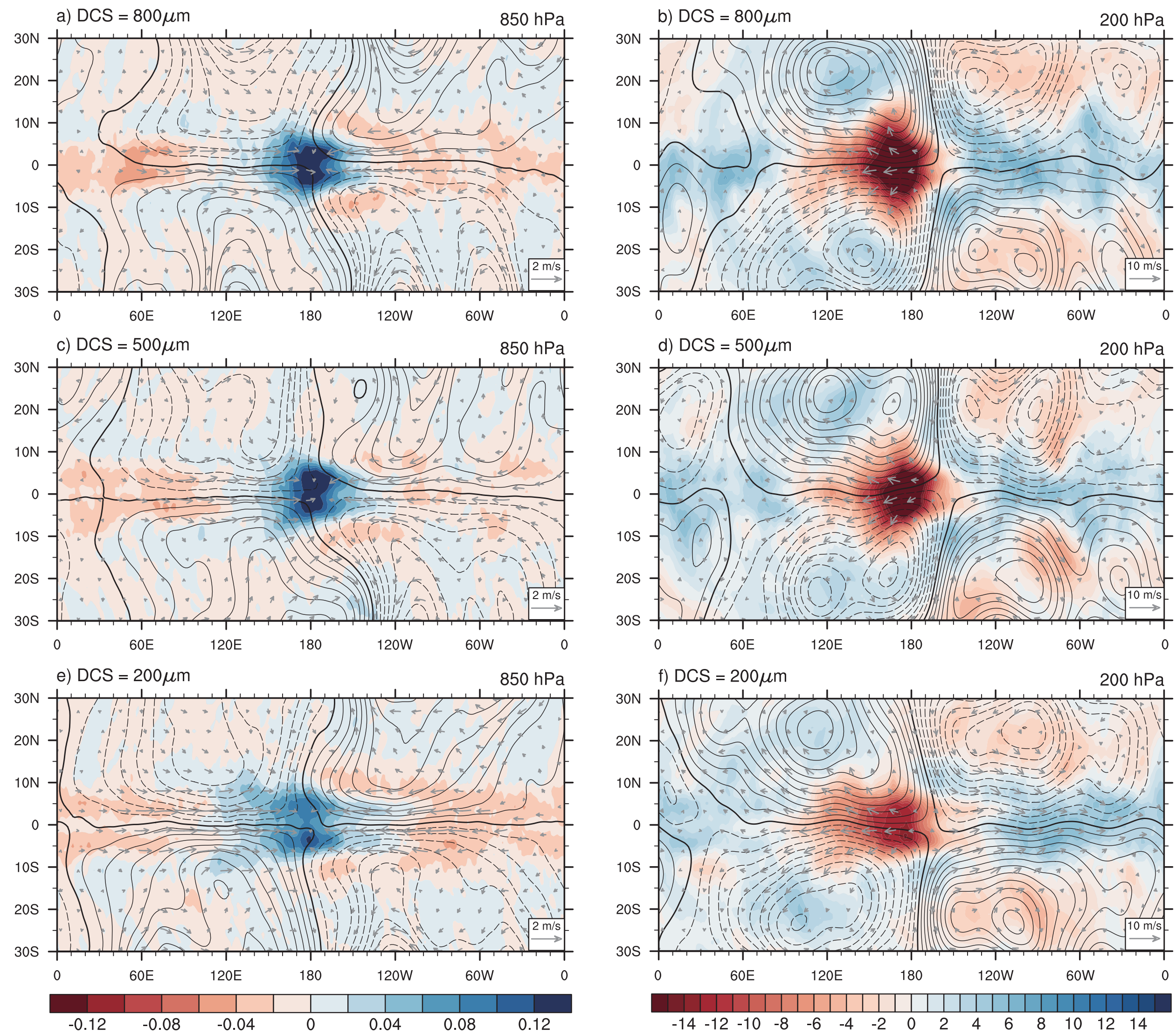

FIG. 8. The regression of (a, c, e) precipitation rate (color, units: mm/hr), (b, d, f) OLR (color, units: W/m^2), wind (vector, units: m/s), and stream function (contour, units: 10^6 m^2/s) onto the MJO index. For wind and stream function, the left column is at approximate 850-hPa, and the right column is at approximate 200-hPa. Dashed contours indicated negative values. Contour intervals for stream function at 850-hPa and 200-hPa are 0.2 10^6 m^2/s and 0.5 10^6 m^2/s, respectively.

With the increasing DCS, the wind vectors near the convective centers show a stronger poleward anomalous transport, indicating a stronger divergence corresponding with the stronger convection.

As for how CRI effects manifest in the horizontal structure of MJO-like mode, the enhancement of precipitation and OLR anomalies at the convective center with the increasing DCS can be seen in Figure 8. Less LW radiation escaping into space means more radiative heating results from the high-level cloud increases. The heavier rainfall and more intense radiative heating imply that the MJO convection intensifies and the MJO precipitation variance increases. In addition, when DCS = 200 μm, the flow field is dominated by wavenumber one, showing a more stable and broader structure than other cases, and the ”swallowtail” shape in the precipitation field has a wider zonal span. Higher-wavenumber disturbances (especially the structure of wavenumber 2-3), by contrast, appear in the flow fields when DCS increases; meanwhile, the "swallowtail" shape shrinks zonally with shorter tails or even disappears. The emergence of higher-wavenumber signals and the smaller-scale patterns are consistent with the implications from the WK99 spectra (Figure 6), likely associated with the enhancement of convection in all scales due to the mean state changes.

The vertical structure of MJO-like mode in our simulations is also shown in the regression maps (Figure 9). We make an average over the deep tropical (5°S-5°N), and similar features can be obtained if the range is expanded to 10°S-10°N. In the intraseasonal scale, the positive cloud fraction anomalies increase at the convective center in the mid- and upper-troposphere. More cloud is produced in the DCS800 experiments, leading to a stronger MJO-associated cloud forcing. The temperature changes mainly occur at the convective center above the middle troposphere, and below the high cloud bottom, illustrated by the changes in air temperature anomalies in Figure 9. The increased temperature anomalies with DCS may come from the stronger radiative heating and stronger latent heating in the MJO centers.

The mass flux vector in Figure 9 measures how the air mass transports vertically. It can be regarded as resolved mass flux, but not the parameterized convective mass flux. In the DCS200 case (Figure 9c), the mass flux has a relative upright updraft at 180° longitude, while the mass flux gradually tilts westward with height as the DCS increases with longer arrows, showing a stronger vertical transport and a stronger mass divergence above the mid-troposphere. It is also evidence supporting the strengthening of MJO convection.

To sum up, the most pronounced changes in the characteristics of MJO-like mode associated with the increasing CRI are 1) intensification, 2) slower propagation, and 3) smaller zonal scale. Such a simulated space-time relationship is consistent with the observational results of Lyu et al. (2021)'s study, which suggests a broader extension of MJO is associated with a faster propagation, and vice

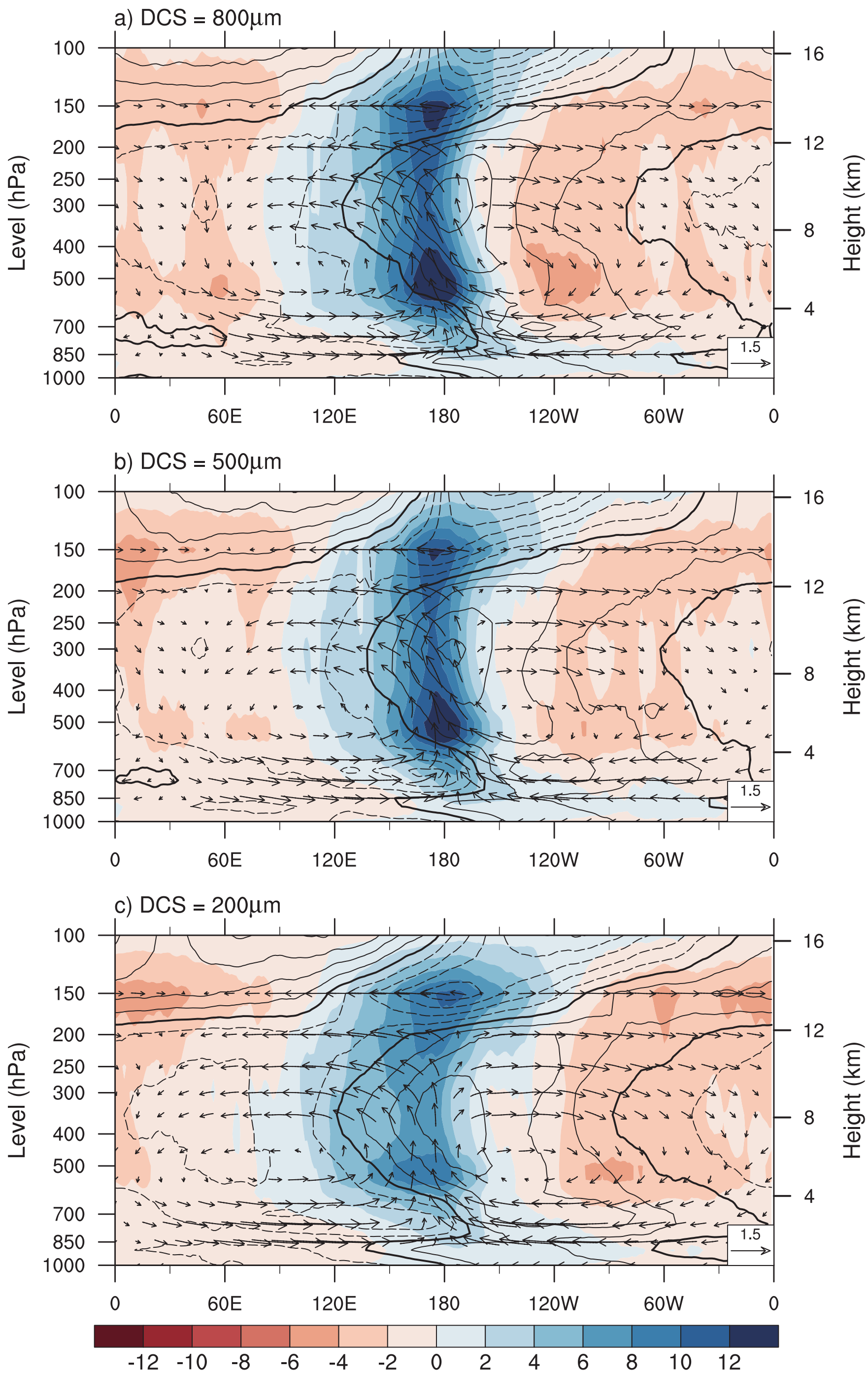

FIG. 9. The vertical regression of cloud fraction (color, units: %), air temperature (contour, units: °C), and mass flux (ρu and ρw, vector, units: kg m^{-2} s^{-1}) within 5°S-5°N onto the MJO index. The dashed contour indicated negative values. The contour interval for temperature is 0.1 °C. ρw is multiplied by a factor of 250.

versa. In the following analysis, we mainly focus on the mechanisms of MJO intensification and slower propagation.

b. Physical Processes Causing the Changes

1) MSE Maintenance and Propagation

The general consensus of previous studies suggests the moisture's importance in MJO mechanisms. To better understand MJO-like mode's maintenance and propagation, we can infer the key processes from the moist static energy (MSE) budget analysis.

The MSE (denoted by h), also referred to as frozen MSE, is defined as

$$h = C_p T + gZ + L_v q - L_f q_i, \tag{3}$$

where C_p is the specific heat at constant pressure, T is the temperature, g is the gravitational acceleration, Z is the height, L_v is the latent heat of vaporization, q is the specific humidity of water vapor, L_f is the latent heat of sublimation and q_i is the specific quantity of ice. The MSE is conserved in moist adiabatic processes. The mass-weighted column-integrated MSE is the integral of MSE from the bottom to the top of the atmospheric column as follows:

$$\langle h \rangle = \int_{p_{\text{top}}}^{p_{\text{sfc}}} h \frac{dp}{g}, \tag{4}$$

where $\langle ... \rangle$ represents the mass-weighted vertical integral, p is the pressure, p_{sfc} is the surface pressure and p_{top} is the pressure at the top of model. The other column-integrated variables all follow this equation.

The column-integrated MSE tendency can be expressed in the budget style:

$$\langle \frac{\partial h}{\partial t} \rangle = -\langle \omega \frac{\partial h}{\partial p} \rangle - \langle \mathbf{V} \cdot \nabla h \rangle + LH + SH + \langle LW \rangle + \langle SW \rangle, \tag{5}$$

where $\mathbf{V}$ is the horizontal wind vector on a pressure level, ∇ is the gradient operator, ω is the pressure velocity, LH and SH are the latent heat flux and the sensible heat flux from the surface into the atmospheric column, and the $\langle LW \rangle$ and $\langle SW \rangle$ are the column-integrated LW and SW radiative heating rates. The term on the left of Equation 5 is the local $\langle h \rangle$ tendency (MSE tendency term). On the right of Equation 5, the first term is column-integrated horizontal advection of h (horizontal advection term), the second term is column-integrated vertical advection of h (vertical advection term) and the rest four terms are the heating sources. The residual term is calculated as the differences between the directly calculated $\langle \partial h/\partial t \rangle$ and the sum of six budget terms to the right of Equation 5, representing the numerical errors.

The patterns of column-integrated MSE anomalies and column-integrated MSE tendency anomalies associated with MJO are shown in Figure 10. The upper row of Figure 10 exhibits positive MSE anomalies at the MJO center with the two dry anomalous regions on both sides of the east and west. This pattern is similar to the precipitation and OLR fields in Figure 8, also reflecting the basic spatial structure of MJO-like mode. The column MSE anomalies at the MJO center increase from DCS200 to DCS800 generally, while the DCS500 case seems to exhibit higher maximum values. In the lower row of Figure 10, the distribution of MJO-regressed column MSE tendency shows approximately a quarter phase difference ahead of column MSE. The MSE tendency has positive anomalies to the east of the convective center with negative anomalies to the west. The configuration of MSE and its tendency anomalies determines the eastward propagation of MJO. When CRI intensifies, the zonal range of strong MSE tendency anomalies shrinks toward the convective center and the amplitude of MSE tendency variance in deep tropics seems to become lower. These changes imply the slower propagation of MJO-like mode, consistent with our previous results.

To examine how the MSE budget terms contribute to the maintenance and propagation of MJO-like mode, we follow the projecting method proposed by Andersen and Kuang (2012). Figure 11 illustrates the calculation results which are the fractional contributions of MJO-regressed MSE budget terms to the MJO-regressed column MSE and MSE tendency. They can be calculated as

$$S_m(x) = \frac{\| x \cdot \langle h \rangle \|}{\| \langle h \rangle^2 \|}, \quad (6)$$

$$S_p(x) = \frac{\| x \cdot \langle \partial h/\partial t \rangle \|}{\| \langle \partial h/\partial t \rangle^2 \|}, \quad (7)$$

where S_m and S_p represent the projection onto the maintenance and propagation respectively, x is MJO-regressed MSE budget term, $\| y \| = \int\int y dA$ is the integral of y over the deep tropics A (5°S-5°N, all longitude). If we enlarge the integral region to 10°S-10°N, similar results are obtained. The sum of six projection terms is named "total" in Figure 11. The differences between

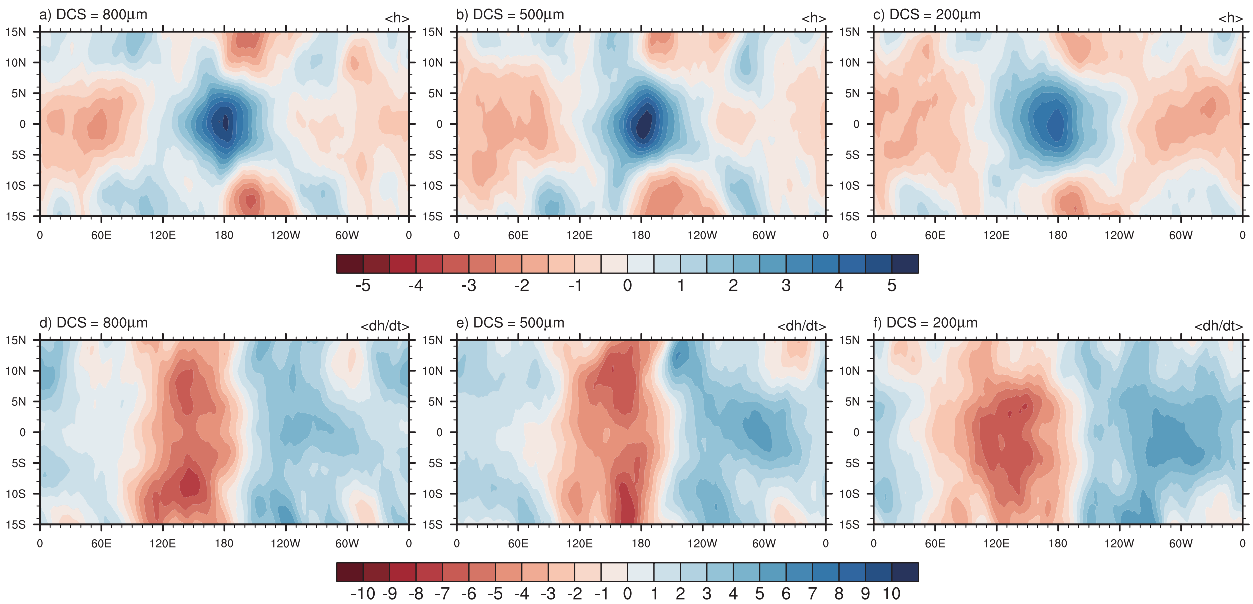

FIG. 10. The regression of (a, b, c) column-integrated MSE (units: 10^6 J/m^2) and (d, e, f) column-integrated MSE tendency (units: 10^5 J m^{-2} day^{-1}) onto the MJO index.

"total" and the MSE tendency term are due to the existence of the residual term. Although the residual term is not small enough to be ignored, it does not affect our qualitative analysis of other terms.

As we can see from Figure 11, the LW radiation term is distinguishable from other sources, contributing to the maintenance of column MSE and slowing down its propagation. The SW radiation term has the same effect, however, its contribution is not significant. Regarding the two terms as total radiative heating source, the MSE budget bar chart obviously highlights the role of CRI in MJO-like mode. When DCS increases, the CRI has a larger positive contribution to the maintenance and a larger negative contribution to the propagation. It is the only term among the MSE budget terms that is well consistent with the characteristic changes of the MJO-like mode, intensifying the MJO-like mode and retarding its eastward propagation with the increasing DCS.

The horizontal advection term is the source for eastward propagation but the sink for maintaining the column MSE. When CRI intensifies, the role of horizontal advection in dissipation weakens, beneficial to the MJO intensification while the contribution of horizontal advection to the propagation barely changes. However, in Figure 11, the vertical advection term is detrimental to the maintenance and accelerates MJO's eastward moving, especially when DCS becomes larger.

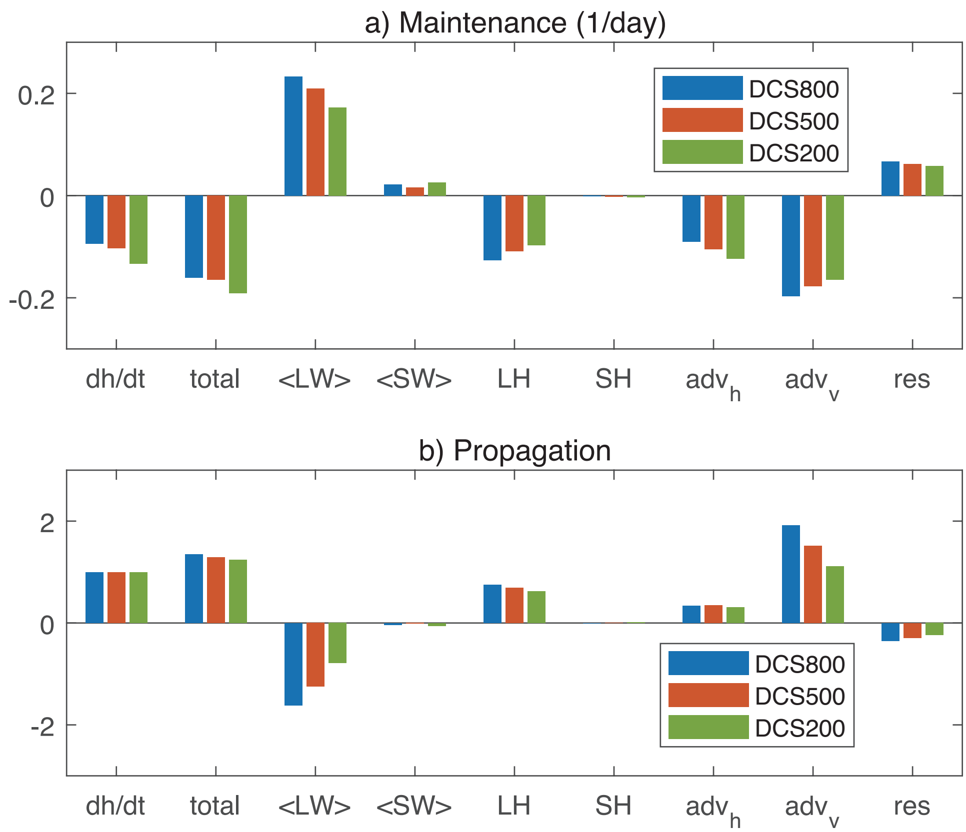

FIG. 11. The projection of MSE budget terms onto the MJO-regressed (a) column MSE and (b) column MSE tendency. The region used for calculation is all longitude within 5°S-5°N

Obviously, such effects are opposite to our simulation results. For the MJO maintenance, the change in the vertical advection contribution with DCS is opposite to the change in horizontal advection contribution, making their effects offset each other and their total effect insignificant in MJO changes. Though the vertical advection term indeed tends to give a faster MJO propagation in DCS800, the radiation tendency still dominates over the advection (take the ratio = 1 as reference).

It is interesting that the latent heat term is a sink of column MSE (Figure 11), while in the WISHE-moisture mode theory represented by Fuchs and Raymond (2017), the WISHE feedback plays a dominant role in the instability growth and propagation acceleration, which particularly has a positive effect on MJO intensity. How to understand such differences is not what this study focuses on, but is worth further investigating in the future.

In conclusion, the MSE budget analysis confirms the crucial role of CRI in changing MJO-like mode in our simulations. The changes in MJO-like mode are dominantly determined by CRI, rather than the dynamic processes associated with the intraseasonal moisture advection.

When DCS increases, the larger cloud fraction with more cloud ice produces more radiative heating in the MJO center, warming the troposphere therein (Figure 9). The DCS-induced radiative feedback exerts direct effects on the intraseasonal variability, driving a stronger moist ascending at the MJO convective center, beneficial to the deep convection and precipitation generation associated with MJO. CRI intensification also decelerates the MJO-like mode, which is mainly because the phase difference between the LW radiative forcing and the MSE tendency (the specific figures are not shown but it can be inferred from the OLR anomalies in Figure 8 and the regressed column MSE tendency anomalies in Figure 10), manifesting as the LW heating center lagging behind the positive MSE tendency center. The stronger LW radiative forcing with increasing DCS consequently intensifies this deceleration.

2) Inferences from Mean State Changes

The CRI not only influence the MJO behavior directly in intraseasonal scale, but also likely influence MJO through the DCS-induced mean state changes.

In Section 3, we find that the DCS-induced CRI intensification warms and moistens the tropics (Figure 2), meanwhile causing a strengthened HC (Figure 3). The changed CRI and atmospheric mean state stimulate cloud-radiative-circulation feedback, which provides favorable conditions for the development of deep convection and generation of convective clouds in tropics, consistent with the power changes in the symmetric WK99 spectra (Figure 6a, 6c, and 6e). In those spectra as well as the background spectra (figure not shown), we can see the power intensifies almost in all spatial-temporal scales.

MJO is an organized convective system traveling in the tropics. In such an environment conducive to convection, MJO is more likely to generate stronger convection and precipitation. As shown in the symmetric WK99 spectra, the power signal within the MJO band becomes stronger as the signals in other scales do. It can be regarded as a pathway that the mean state change influences MJO.

What's more, the subtropical mid-troposphere dries as we increase DCS (Figure 2d-f). This enhances meridional moisture gradient, and might further accelerate MJO propagation based on Kang et al. (2021), who discuss the MJO propagation over the Maritime Continent in boreal winter. However, the changes in MJO propagation in our simulations are inconsistent with Kang et al. (2021). Our idealized simulations without zonal asymmetry, seasonal cycle, and land-sea distribution may partially account for this discrepancy, which is worth further investigation.

5. Summary and Discussion

This study investigates how CRI affects tropical mean state and MJO-like mode by tuning a sensitive cloud microphysics parameter (DCS) in the CESM2 aquaplanet model. The findings suggest that DCS-induced CRI changes play a crucial role in altering the mean state and modulating the MJO characteristics.

Turning DCS larger results in the changes in cloud properties, leading to more high clouds with a stronger CRI. It greatly changes the tropical mean state by increasing the tropospheric temperature and moisture in the tropics, increasing the meridional heat and moisture gradient, as well as strengthening the Hadley circulation and trade winds. The tropical precipitation and cloud radiative forcing are also enhanced under the CRI intensification. On the one hand, the mean state changes in our simulations can be explained by the direct role of cloud microphysics parameterization changes. On the other hand, the mean state changes with CRI can be also elucidated from the so-called cloud-radiative-circulation feedback. The DCS-induced mean state changes create a favorable environment for deep convections, generating more convective clouds. The CRI, thereby, can be also strengthened via cloud-radiative-circulation feedback, which is a different pathway from the manual parameter tuning.

The unique role of DCS in cloud forcing and precipitation is also examined from the probability density function. Increasing DCS strongly affects the extreme cloud forcing (larger than 100 W/m^2), and shifts the median of precipitation PDF to a heavier precipitation range. As to the relationship between them (call it R-P relation), it exhibits a non-linear "S" shape. If the cloud forcing and precipitation are near the median, the cloud forcing grows faster with increasing precipitation when DCS is larger, leading to a stronger cloud-radiative effect per unit precipitation. However, the cloud forcing saturates when precipitation is very strong, which indicates that the cloud forcing has its limit and the effect of tuning DCS is also limited when the DCS value is over a reasonable range.

The DCS-induced CRI changes can also influence the MJO-like mode characterized by eastward propagation, wavenumber-1 features, and a 20-100-day period. With the strengthened CRI, the MJO-like mode intensifies and propagates more slowly with a lower frequency. According to the MSE budget analysis, the CRI, especially the LW radiative forcing, directly influences MJO on the intraseasonal scale, dominating its intensity and propagation changes. With the increasing DCS, LW radiative heating has a larger positive contribution to MJO maintenance and a larger negative contribution to MJO eastward propagation. As to other terms in the MSE budget, some of them offset each other, some of them barely change, and some of them are opposite to our simulation results. The role of CRI can be also explained as follows: when strengthening CRI, more clouds, more precipitation, stronger radiative heating, and stronger upward motion are diagnosed at the MJO convective center, supporting the intensification of MJO-like mode. The phase difference between LW heating and MSE tendency accounts for the deceleration.

The CRI not only influences MJO directly on the intraseasonal scale but also influences MJO through the DCS-induced mean state changes. The mean state changed by CRI intensification provides a warmer, moister tropical atmosphere with stronger HC, beneficial to the tropical convection in all spatial-temporal scales, including the convection within "MJO band" shown in WK99 spectra.

It needs to emphasize the special method that simply uses the DCS parameter to control the CRI. It provides a novel perspective for considering the effects of CRI. However, the DCS parameter behaves with different values in different models (Zhang et al. 2013; Fan et al. 2021) and is chosen arbitrarily (Eidhammer et al. 2014) due to no physical and observational basis (Eidhammer et al. 2017). Efforts are underway to address this uncertainty. It may be worth exploring the realistic conditions under which DCS can increase to establish a connection between DCS and the real world before new approaches replace the "auto-conversion" in parameterization schemes.

As discussed before, we observe disparities in the WISHE effect on MJO based on different analyzing methods: Andersen and Kuang (2012) and Fuchs and Raymond (2017). The latter supports the view that WISHE feedback plays a dominant role in instability growth and propagation acceleration in a linearized model. A recent review paper (Jiang et al. 2020) categorizes these two theories into different groups by the criterion that whether CRI or WISHE determines the MJO features. However, the reasons for such disparities and which mechanism, CRI or WISHE, determines MJO have not been answered yet and lack consensus. One suspicion is that the disparities are the discrepancies between linearized models with growing modes and the nonlinear numerical models with steady-state disturbances. It also warrants further investigation.

Acknowledgments. The work described in this paper was substantially supported by a grant from the Research Grants Council of the Hong Kong Special Administrative Region, China (Project Reference Number: AoE/P-601/23-N) and the Center for Ocean Research in Hong Kong and Macau (CORE), a joint research center between the Laoshan Laboratory and Technology and the Hong Kong University of Science and Technology (HKUST). The supercomputer Tianhe-2 used for computation is provided by National Supercomputer Center in Guangzhou, China. DK was supported by New Faculty Startup Fund from Seoul National University, NASA MAP program (80NSSC21K1495), NOAA MAPP program (NA21OAR4310343), NOAA CVP program (NA22OAR4310608), and KMA R&D program (KMI2021-01210)

Data availability statement. The CESM2 model can be accessed from the official website (https://www.cesm.ucar.edu/models/cesm2/). Due to the substantial data size, cloud-storage for our simulation data is inconvenient. For inquiries about accessing our simulation data, please contact us for sharing.

References

Adames, Á. F., and J. M. Wallace, 2014: Three-Dimensional Structure and Evolution of the MJO and Its Relation to the Mean Flow. *Journal of the Atmospheric Sciences*, **71 (6)**, 2007–2026, https://doi.org/10.1175/JAS-D-13-0254.1.

Adames, Á. F., and J. M. Wallace, 2015: Three-Dimensional Structure and Evolution of the Moisture Field in the MJO. *Journal of the Atmospheric Sciences*, **72 (10)**, 3733–3754, https://doi.org/10.1175/JAS-D-15-0003.1.

Andersen, J. A., and Z. Kuang, 2012: Moist Static Energy Budget of MJO-like Disturbances in the Atmosphere of a Zonally Symmetric Aquaplanet. *Journal of Climate*, **25 (8)**, 2782–2804, https://doi.org/10.1175/JCLI-D-11-00168.1.

Benedict, J. J., B. Medeiros, A. C. Clement, and J. G. Olson, 2020: Investigating the Role of Cloud-Radiation Interactions in Subseasonal Tropical Disturbances. *Geophysical Research Letters*, **47 (9)**, https://doi.org/10.1029/2019GL086817.

Bischoff, T., and T. Schneider, 2016: The Equatorial Energy Balance, ITCZ Position, and Double-ITCZ Bifurcations. *Journal of Climate*, **29 (8)**, 2997–3013, https://doi.org/10.1175/JCLI-D-15-0328.1.

Bogenschutz, P. A., A. Gettelman, C. Hannay, V. E. Larson, R. B. Neale, C. Craig, and C.-C. Chen, 2018: The path to CAM6: Coupled simulations with CAM5.4 and CAM5.5. *Geoscientific Model Development*, **11 (1)**, 235–255, https://doi.org/10.5194/gmd-11-235-2018.

Ceppi, P., and D. L. Hartmann, 2015: Connections Between Clouds, Radiation, and Midlatitude Dynamics: A Review. *Current Climate Change Reports*, **1 (2)**, 94–102, https://doi.org/10.1007/s40641-015-0010-x.

Ceppi, P., Y.-T. Hwang, X. Liu, D. M. W. Frierson, and D. L. Hartmann, 2013: The relationship between the ITCZ and the Southern Hemispheric eddy-driven jet. *Journal of Geophysical Research: Atmospheres*, **118 (11)**, 5136–5146, https://doi.org/10.1002/jgrd.50461.

Ceppi, P., M. D. Zelinka, and D. L. Hartmann, 2014: The response of the Southern Hemispheric eddy-driven jet to future changes in shortwave radiation in CMIP5. *Geophysical Research Letters*, **41 (9)**, 3244–3250, https://doi.org/10.1002/2014GL060043.

Crueger, T., and B. Stevens, 2015: The effect of atmospheric radiative heating by clouds on the Madden-Julian Oscillation. *Journal of Advances in Modeling Earth Systems*, **7 (2)**, 854–864, https://doi.org/10.1002/2015MS000434.

Eidhammer, T., H. Morrison, A. Bansemer, A. Gettelman, and A. J. Heymsfield, 2014: Comparison of ice cloud properties simulated by the Community Atmosphere Model (CAM5) with in-situ observations. *Atmospheric Chemistry and Physics*, **14 (18)**, 10 103–10 118, https://doi.org/10.5194/acp-14-10103-2014.

Eidhammer, T., H. Morrison, D. Mitchell, A. Gettelman, and E. Erfani, 2017: Improvements in Global Climate Model Microphysics Using a Consistent Representation of Ice Particle Properties. *Journal of Climate*, **30 (2)**, 609–629, https://doi.org/10.1175/JCLI-D-16-0050.1.

Fan, Y., Y. T. Chung, and X. Shi, 2021: The Essential Role of Cloud-Radiation Interaction in Non-rotating Convective Self-Aggregation. *Geophysical Research Letters*, **48 (19)**, e2021GL095 102, https://doi.org/10.1029/2021GL095102.

Fuchs, Ž., and D. J. Raymond, 2002: Large-Scale Modes of a Nonrotating Atmosphere with Water Vapor and Cloud–Radiation Feedbacks. *Journal of the Atmospheric Sciences*, **59 (10)**, 1669–1679, https://doi.org/10.1175/1520-0469(2002)059⟨1669:LSMOAN⟩2.0.CO;2.

Fuchs, Z., and D. J. Raymond, 2005: Large-Scale Modes in a Rotating Atmosphere with Radiative–Convective Instability and WISHE. *Journal of the Atmospheric Sciences*, **62 (11)**, 4084–4094, https://doi.org/10.1175/JAS3582.1.

Fuchs, Ž., and D. J. Raymond, 2017: A simple model of intraseasonal oscillations. *Journal of Advances in Modeling Earth Systems*, **9 (2)**, 1195–1211, https://doi.org/10.1002/2017MS000963.

Fuchs-Stone, Ž., 2020: WISHE-Moisture Mode in a Vertically Resolved Model. *Journal of Advances in Modeling Earth Systems*, **12 (2)**, e2019MS001 839, https://doi.org/10.1029/2019MS001839.

Gettelman, A., and H. Morrison, 2015: Advanced Two-Moment Bulk Microphysics for Global Models. Part I: Off-Line Tests and Comparison with Other Schemes. *Journal of Climate*, **28 (3)**, 1268–1287, https://doi.org/10.1175/JCLI-D-14-00102.1.

Golaz, J.-C., V. E. Larson, and W. R. Cotton, 2002: A PDF-Based Model for Boundary Layer Clouds. Part I: Method and Model Description. *Journal of the Atmospheric Sciences*, **59 (24)**, 3540–3551, https://doi.org/10.1175/1520-0469(2002)059⟨3540:APBMFB⟩2.0.CO;2.

Harrop, B. E., and D. L. Hartmann, 2016: The Role of Cloud Radiative Heating in Determining the Location of the ITCZ in Aquaplanet Simulations. *Journal of Climate*, **29 (8)**, 2741–2763, https://doi.org/10.1175/JCLI-D-15-0521.1.

Iacono, M. J., J. S. Delamere, E. J. Mlawer, M. W. Shephard, S. A. Clough, and W. D. Collins, 2008: Radiative forcing by long-lived greenhouse gases: Calculations with the AER radiative transfer models. *Journal of Geophysical Research: Atmospheres*, **113 (D13)**, https://doi.org/10.1029/2008JD009944.

Jiang, X., and Coauthors, 2020: Fifty Years of Research on the Madden-Julian Oscillation: Recent Progress, Challenges, and Perspectives. *Journal of Geophysical Research: Atmospheres*, **125 (17)**, https://doi.org/10.1029/2019JD030911.

Kang, D., D. Kim, M.-S. Ahn, and S.-I. An, 2021: The Role of the Background Meridional Moisture Gradient on the Propagation of the MJO over the Maritime Continent. *Journal of Climate*, **34 (16)**, 6565–6581, https://doi.org/10.1175/JCLI-D-20-0085.1.

Kim, D., M.-S. Ahn, I.-S. Kang, and A. D. Del Genio, 2015: Role of Longwave Cloud–Radiation Feedback in the Simulation of the Madden–Julian Oscillation. *Journal of Climate*, **28 (17)**, 6979–6994, https://doi.org/10.1175/JCLI-D-14-00767.1.

Larson, V. E., J.-C. Golaz, and W. R. Cotton, 2002: Small-Scale and Mesoscale Variability in Cloudy Boundary Layers: Joint Probability Density Functions. *Journal of the Atmospheric Sciences*, **59 (24)**, 3519–3539, https://doi.org/10.1175/1520-0469(2002)059⟨3519:SSAMVI⟩2.0.CO;2.

Lee, M.-I., I.-S. Kang, J.-K. Kim, and B. E. Mapes, 2001: Influence of cloud-radiation interaction on simulating tropical intraseasonal oscillation with an atmospheric general circulation model. *Journal of Geophysical Research: Atmospheres*, **106 (D13)**, 14 219–14 233, https://doi.org/10.1029/2001JD900143.

Leroux, S., and Coauthors, 2016: Inter-model comparison of subseasonal tropical variability in aquaplanet experiments: Effect of a warm pool. *Journal of Advances in Modeling Earth Systems*, **8 (4)**, 1526–1551, https://doi.org/10.1002/2016MS000683.

Li, Y., D. W. J. Thompson, and S. Bony, 2015: The Influence of Atmospheric Cloud Radiative Effects on the Large-Scale Atmospheric Circulation. *Journal of Climate*, **28 (18)**, 7263–7278, https://doi.org/10.1175/JCLI-D-14-00825.1.

Lyu, M., X. Jiang, Z. Wu, D. Kim, and Á. F. Adames, 2021: Zonal-Scale of the Madden-Julian Oscillation and Its Propagation Speed on the Interannual Time-Scale. *Geophysical Research Letters*, **48 (6)**, e2020GL091 239, https://doi.org/10.1029/2020GL091239.

Madden, R. A., and P. R. Julian, 1971: Detection of a 40–50 Day Oscillation in the Zonal Wind in the Tropical Pacific. *Journal of the Atmospheric Sciences*, **28 (5)**, 702–708, https://doi.org/10.1175/1520-0469(1971)028⟨0702:DOADOI⟩2.0.CO;2.

Maloney, E. D., A. H. Sobel, and W. M. Hannah, 2010: Intraseasonal variability in an aquaplanet general circulation model. *Journal of Advances in Modeling Earth Systems*, **2**, 5, https://doi.org/10.3894/JAMES.2010.2.5.

Medeiros, B., D. L. Williamson, and J. G. Olson, 2016: Reference aquaplanet climate in the Community Atmosphere Model, Version 5. *Journal of Advances in Modeling Earth Systems*, **8 (1)**, 406–424, https://doi.org/10.1002/2015MS000593.

Morrison, H., and A. Gettelman, 2008: A New Two-Moment Bulk Stratiform Cloud Microphysics Scheme in the Community Atmosphere Model, Version 3 (CAM3). Part I: Description and Numerical Tests. *Journal of Climate*, **21 (15)**, 3642–3659, https://doi.org/10.1175/2008JCLI2105.1.

Pathak, R., S. Sahany, and S. K. Mishra, 2020: Uncertainty quantification based cloud parameterization sensitivity analysis in the NCAR community atmosphere model. *Scientific Reports*, **10 (1)**, 17 499, https://doi.org/10.1038/s41598-020-74441-x.

Rushley, S. S., D. Kang, D. Kim, S.-I. An, and T. Wang, 2023: MJO in Different Orbital Regimes: Role of the Mean State on the MJO's Amplitude during Boreal Winter. *Journal of Climate*, **-1 (aop)**, 1–41, https://doi.org/10.1175/JCLI-D-22-0725.1.

Shaw, T. A., 2019: Mechanisms of Future Predicted Changes in the Zonal Mean Mid-Latitude Circulation. *Current Climate Change Reports*, **5 (4)**, 345–357, https://doi.org/10.1007/s40641-019-00145-8.

Shi, X., D. Kim, Á. F. Adames, and J. Sukhatme, 2018: WISHE-Moisture Mode in an Aquaplanet Simulation. *Journal of Advances in Modeling Earth Systems*, **10 (10)**, 2393–2407, https://doi.org/10.1029/2018MS001441.

Sobel, A., and E. Maloney, 2012: An Idealized Semi-Empirical Framework for Modeling the Madden–Julian Oscillation. *Journal of the Atmospheric Sciences*, **69 (5)**, 1691–1705, https://doi.org/10.1175/JAS-D-11-0118.1.

Tao, W.-K., S. Lang, J. Simpson, C.-H. Sui, B. Ferrier, and M.-D. Chou, 1996: Mechanisms of Cloud-Radiation Interaction in the Tropics and Midlatitudes. *Journal of the Atmospheric Sciences*, **53 (18)**, 2624–2651, https://doi.org/10.1175/1520-0469(1996)053⟨2624:MOCRII⟩2.0.CO;2.

Tian, B., and V. Ramanathan, 2003: A Simple Moist Tropical Atmosphere Model: The Role of Cloud Radiative Forcing. *Journal of Climate*, **16 (12)**, 2086–2092, https://doi.org/10.1175/1520-0442(2003)016⟨2086:ASMTAM⟩2.0.CO;2.

Wheeler, M., and G. N. Kiladis, 1999: Convectively Coupled Equatorial Waves: Analysis of Clouds and Temperature in the Wavenumber–Frequency Domain. *Journal of the Atmospheric Sciences*, **56 (3)**, 374–399, https://doi.org/10.1175/1520-0469(1999)056⟨0374:CCEWAO⟩2.0.CO;2.

Williamson, L., and Coauthors, 2012: The APE atlas. https://doi.org/10.5065/D6FF3QBR.

Zhang, C., 2005: Madden-Julian Oscillation. *Reviews of Geophysics*, **43 (2)**, https://doi.org/10.1029/2004RG000158.

Zhang, C., and J. Ling, 2012: Potential Vorticity of the Madden–Julian Oscillation. *Journal of the Atmospheric Sciences*, **69 (1)**, 65–78, https://doi.org/10.1175/JAS-D-11-081.1.

Zhang, G. J., and N. A. McFarlane, 1995: Sensitivity of climate simulations to the parameterization of cumulus convection in the Canadian climate centre general circulation model. *Atmosphere-Ocean*, **33 (3)**, 407–446, https://doi.org/10.1080/07055900.1995.9649539.

Zhang, K., X. Liu, M. Wang, J. M. Comstock, D. L. Mitchell, S. Mishra, and G. G. Mace, 2013: Evaluating and constraining ice cloud parameterizations in CAM5 using aircraft measurements from the SPARTICUS campaign. *Atmospheric Chemistry and Physics*, **13 (9)**, 4963–4982, https://doi.org/10.5194/acp-13-4963-2013.

Zhao, C., and Coauthors, 2013: A sensitivity study of radiative fluxes at the top of atmosphere to cloud-microphysics and aerosol parameters in the community atmosphere model CAM5. *Atmospheric Chemistry and Physics*, **13 (21)**, 10 969–10 987, https://doi.org/10.5194/acp-13-10969-2013.